Journal of Zhejiang University-SCIENCE B 2025 26(12):1156-1171
www.jzus.zju.edu.cn; www.springer.com/journal/11585
E-mail: jzus_b@zju.edu.cn

Research Article
https://doi.org/10.1631/jzus.B2500343

Novel multi-component synergistic bioink that balances biocompatibility and mechanical strength for cartilage regeneration

Zijun MA[1], Wendan JIA[1], Xiaoyuan WANG[1], Rong CHENG[1], Lu HAN[1], Meng LI[1]✉, Xiaoning YANG[3]✉, Shengbo SANG[1,2]✉

[1]*Shanxi Key Laboratory of Artificial Intelligence & Micro Nano Sensors, College of Integrated Circuits, Taiyuan University of Technology, Taiyuan 030024, China*
[2]*Key Lab of Advanced Transducers and Intelligent Control System of the Ministry of Education, Taiyuan University of Technology, Taiyuan 030024, China*
[3]*Shanxi-Zheda Institute of Advanced Materials and Chemical Engineering, Taiyuan 030024, China*

Abstract: Hydrogels, owing to their porous network structure resembling the extracellular matrix (ECM), have become essential scaffold materials in the field of cartilage tissue engineering. Among them, gelatin methacrylate (GelMA) hydrogels are widely used in bioink development due to their excellent biocompatibility, biodegradability, and tunable photo-crosslinking properties. However, the high biocompatibility of pure GelMA often comes at the cost of mechanical strength, limiting its applicability in cartilage regeneration. To overcome this trade-off, this study developed composite bioinks based on GelMA, silk fibroin (SF), and polyethylene oxide (PEO) for fabricating porous hydrogel scaffolds, which were then systematically characterized in terms of morphology, porosity, hydrophilicity, mechanical strength, rheological behavior, printability, and cytocompatibility. In this design, PEO serves as a porogen to generate highly porous structures (porosity up to 88%), while SF compensates for the mechanical loss caused by PEO, enabling the scaffold to retain a compression strength of up to 29.10 kPa. Among the tested formulations, the 10% GelMA/1% SF/1.5% PEO (1%=0.01 g/mL) bioink exhibited excellent printability, mechanical integrity, and cytocompatibility, and it supported a robust deposition of collagen II and aggrecan by chondrocytes after printing. This work provides a versatile strategy for balancing the biocompatibility and mechanical robustness in bioinks, offering a promising platform for next-generation cartilage tissue engineering scaffolds.

Key words: Silk fibroin; Polyethylene oxide; Multi-component collaboration; Cartilage regeneration; Tissue engineering

1 Introduction

Articular cartilage defects resulting from trauma, surgical resection, or degenerative conditions pose a significant therapeutic challenge in orthopaedics due to their low intrinsic healing capacity (Shi et al., 2022; Xia et al., 2022; Xue NN et al., 2022; Yuan et al., 2024). More specifically, defects that exceed a critical size, typically defined as those with a diameter greater than 2 cm, cannot undergo effective self-repair, often resulting in non-union or the formation of structurally and functionally inadequate tissue (Zhang et al., 2020; Findeisen et al., 2023). Current clinical strategies rely mainly on autografts and allografts (Müller et al., 2016; Tuchman et al., 2016); however, these approaches face substantial limitations, including donor site morbidity, limited tissue availability, and the risks of immune rejection and disease transmission (de Girolamo et al., 2019; Liu et al., 2022; He et al., 2024). These constraints have motivated the development of engineered scaffolds that replicate the key structural and biological features of native cartilage (Wang et al., 2020; Lee et al., 2022; Manohar et al., 2024). To fabricate such complex scaffolds, three-dimensional (3D) bioprinting has gained widespread recognition as an emerging technology for creating in vitro biomimetic models, especially in the fields of

✉ Meng LI, mengli_1217@163.com
Xiaoning YANG, xnyang@pku.edu.cn
Shengbo SANG, sunboa-sang@tyut.edu.cn
Meng LI, https://orcid.org/0000-0001-9487-0821
Xiaoning YANG, https://orcid.org/0009-0001-0488-7556
Shengbo SANG, https://orcid.org/0000-0003-3011-7632
Zijun MA, https://orcid.org/0009-0008-4082-3307

Received June 17, 2025; Revision accepted Oct. 4, 2025; Crosschecked Nov. 27, 2025

cartilage tissue engineering and organoid model construction (Wang YT et al., 2024; Bai et al., 2025; Ma et al., 2025).

Bioink plays a crucial role in 3D bioprinting, as its performance directly affects the printing results and subsequent applications. Many researchers have noted that different printing methods have significantly different requirements regarding the performance of bioinks. For example, Ng et al. (2023) investigated the effects of the properties of polyvinylpyrrolidone-based bioink on printing performance and cell proliferation during the inkjet bioprinting process. In addition, Yang et al. (2023) summarized the key characteristics and improvement strategies of gelatin bioink in the extrusion printing process and looked forward to the development direction of functional ink for constructing more complex tissue structures.

Hydrogels have emerged as promising bioinks in the field of 3D bioprinting due to their high water content and porous network structure, which resemble extracellular matrix (ECM) and support nutrient diffusion and cell infiltration (Liu et al., 2017; Zhang et al., 2021). Gelatin methacrylate (GelMA), in particular, has been widely used in scaffold fabrication because of its excellent biocompatibility, biodegradability, and controllable photo-crosslinking properties (Sharifi et al., 2021; Chen et al., 2023). For instance, Wang Z et al. (2024) designed an in vitro shCav3.3 ATDC5-loaded GelMA hydrogel model, providing a new strategy for simulating the endochondral ossification (EO) process in bone organoids. Jeong et al. (2024) successfully prepared an oxygen-generating microparticle (OMP) colloidal bioink for printing using GelMA/gelatin/polyethylene oxide (PEO) and OMP. This bioink has shown potential in solving the oxygen deficiency problem of large printing scaffolds. However, the mechanical and biological performances of this bioink are strongly dependent on its concentration: high concentrations yield dense networks with superior mechanical strength but restrict nutrient transport and waste removal, thereby compromising cell viability (Arguchinskaya et al., 2023); in contrast, low concentrations offer better conditions for cell proliferation and differentiation, yet the resulting scaffold suffers from poor mechanical integrity and has limited printability (Xie et al., 2019).

In order to address the above challenges, PEO has been introduced into GelMA hydrogels to induce microporosity and enhance mass transport. This strategy supports essential cellular processes such as proliferation and migration (Brunel et al., 2022). For example, Jia et al. (2022) developed a photopolymerizable GelMA/PEO bioink that successfully regenerated auricular cartilage with high shape fidelity and ECM deposition. Similarly, Ying et al. (2018) used 3D printing to fabricate porous GelMA/PEO hydrogels that promoted cell viability and maintained structural stability. Nonetheless, while the incorporation of PEO improves porosity and cell performance, it significantly reduces the mechanical strength of the scaffold, limiting its broader applicability in load-bearing contexts.

In order to mitigate the above drawbacks, mechanically robust biomaterials have been investigated. Silk fibroin (SF), a natural protein with outstanding mechanical properties and biocompatibility, has been widely explored in tissue engineering (Zheng et al., 2023). Combining SF with GelMA has been shown to enhance mechanical strength without compromising biological function or printability. Xue YM et al. (2022) reported a nanofibrous SF-GelMA scaffold with improved mechanical and biological performance, while Hou et al. (2023) developed a composite scaffold incorporating melatonin that exhibited enhanced biomechanical characteristics and chondrogenic potential.

In this study, a porous biomimetic scaffold composed of GelMA, PEO, and SF was constructed to achieve both desirable porosity and high mechanical strength (Fig. 1). PEO was employed to introduce a highly porous internal structure, while SF was added to reinforce mechanical stability. Subsequently, the scaffold's porosity, compressive modulus, swelling behavior, rheological properties, printability, and cytocompatibility were systematically characterized, and the optimal GelMA/SF/PEO formulation was identified for 3D printing. Chondrocyte behaviors, including viability, adhesion, and cartilage matrix formation, were further assessed through live/dead staining, cytoskeletal visualization, and immunofluorescence assay. This work presents a versatile strategy for engineering porous hydrogel scaffolds with tunable mechanical and biological properties suitable for cartilage regeneration.

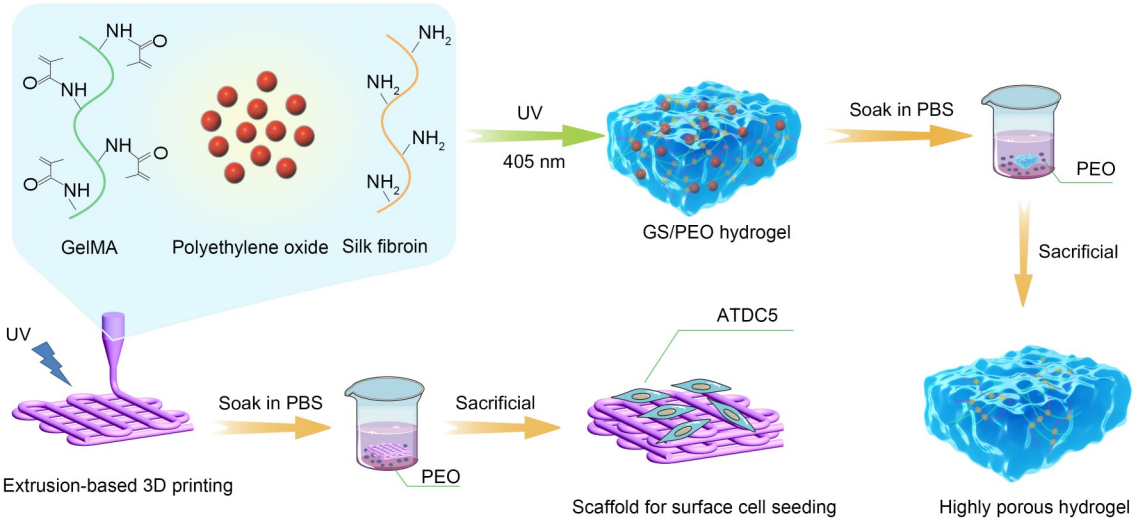

Fig. 1 Schematic of the preparation of GS/PEO porous hydrogel and the printing of 3D scaffolds. GelMA, G: gelatin methacrylate; S: silk fibroin; PEO: polyethylene oxide; PBS: phosphate-buffered saline; UV: ultraviolet; ATDC5: mouse chondrogenic progenitor cells.

2 Materials and methods

2.1 Synthesis of GelMA

The synthesis of GelMA was performed following the protocol reported by Cao et al. (2021). Briefly, 10 g of gelatin (Macklin, Shanghai, China) was dissolved in phosphate-buffered saline (PBS) at a concentration of 10% (volume fraction). Subsequently, 8 mL of methacrylic anhydride (MA; Macklin) was added to the gelatin solution at 500 μL/min over 16 min. After 2 h of reaction time, 400 mL of PBS was added to the mixture to dilute and terminate the reaction. The resulting solution was transferred to a dialysis membrane (molecular weight cutoff: 8000–14 000 Da) and dialyzed against distilled water for 7 d to remove unreacted components. The dialyzed solution was then centrifuged at 4000 r/min for 10 min to remove insoluble residues. The supernatant was collected, lyophilized, and stored at −20 °C until further use. The degree of methacrylation (DoM) of GelMA obtained by this synthesis method was characterized by ^{1}H nuclear magnetic resonance (NMR) as 58.95% (Li et al., 2024).

2.2 In vitro culture of mouse chondrocytes

Mouse chondrogenic progenitor cells (ATDC5) were provided by Wuhan Ponosi Life Technology Co., Ltd. (Wuhan, China), cultivated in Dulbecco's modified Eagle's medium (DMEM)/F12 containing 10% (volume fraction) fetal bovine serum (FBS) and 1% (volume fraction) penicillin/streptomycin, and incubated at 37 °C with 5% CO_2.

2.3 Preparation of the GS/PEO bioink

Different amounts of PEO (Macklin; molecular weight (MW)=100 000 Da, polydispersity index (PDI)=1.13), GelMA, SF, and 0.3% (volume fraction) lithium phenyl-(2,4,6-trimethylbenzoyl) phosphinate (LAP) were dissolved in PBS to prepare bioinks with final GelMA/SF/PEO concentrations of 10%/1%/0%, 10%/1%/0.5%, 10%/1%/1.0%, and 10%/1%/1.5% (1%=0.01 g/mL), and these formulations were designated as GS/0PEO, GS/0.5PEO, GS/1.0PEO, and GS/1.5PEO, respectively. The bioinks were cast into cylindrical molds and exposed to ultraviolet (UV) blue light (405 nm, 5 mW/cm^2) for 1 min to form hydrogels with a height of 6 mm and a diameter of 9 mm for subsequent characterization.

For the bioinks used for cell seeding, the preparation followed the same procedure as described above, except that PEO, GelMA, SF, and 0.3% LAP were dissolved in DMEM/F12. The pH was adjusted to 7 using 1 mmol/L NaOH, and the solution was filtered through a 0.22 μm membrane filter.

2.4 Preparation of GS/1.0PEO bioinks with different molecular weights of PEO

PEO of different molecular weights, GelMA, SF, and 0.3% LAP were dissolved in PBS to prepare

bioinks with the final concentration of GelMA/SF/PEO being 10%/1%/1.0%. The PEO molecular weights used were 12000 Da (Macklin; PDI=1.05), 100000 Da, and 300000 Da (Macklin; PDI=1.04), and these formulations were designated GS/1.0PEO$_{MW=12\,000}$, GS/1.0PEO$_{MW=100\,000}$ and GS/1.0PEO$_{MW=300\,000}$, respectively. The bioinks were cast into cylindrical molds and exposed to blue light for 1 min to form hydrogels with a height of 6 mm and a diameter of 9 mm for subsequent characterization.

For the bioinks used for studying printability, the preparation followed the same procedure as described above.

2.5 Gel permeation chromatography characterization

The molecular weight of GelMA was measured by the gel permeation chromatography (GPC) system (Agilent 1260 Infinity II GPC/SEC system). Briefly, 10 g of GelMA was dissolved in PBS at 10% (volume fraction). Subsequently, the GelMA solution was filtered using a 0.22 μm filter and finally injected into the chromatographic column. During the experiment, the testing temperature was 45 °C, the solvent was 0.1 mol/L $NaNO_3$, and the solvent flow rate was 1 mL/min.

2.6 Fourier transform infrared characterization

GS/PEO hydrogels were freeze-dried and ground into powder for Fourier transform infrared (FTIR) analysis. The scanning spectral range of the infrared spectrometer was set to 4000–400 cm^{-1}, and the resolution was set to 4 cm^{-1}.

2.7 Morphology observation

The prepared cylindrical hydrogels were immersed in PBS for 24 h to remove the PEO from the GS/PEO hydrogels, forming a porous structure. The hydrogel samples were freeze-dried and sectioned using a blade. The cross-sections were fixed on the sample stage and sputter-coated with gold for 45 s. The microstructures of the samples were observed using a scanning electron microscope (SU8010, HITACHI, Japan) at an accelerating voltage of 5 kV. Pore size and porosity were quantified using ImageJ software based on scanning electron microscopy (SEM) images, with three samples analyzed per group.

2.8 Swelling analysis

Lyophilized GS/PEO hydrogels were weighed to obtain their dry weights. The hydrogels were then immersed in PBS and retrieved at predetermined time intervals (1, 2, 3, 4, 5, 7, 9, 11, 18, 24, 30, 36, 42, and 48 h). At each time point, the cylindrical hydrogels were gently blotted with sterile wipes to remove any excess surface PBS, and the wet weight was recorded. The swelling ratio (R_s, %) was calculated using the following formula (Verma et al., 2007):

$$R_s = \frac{W_s - W_d}{W_d} \times 100\%, \tag{1}$$

where W_d and W_s are dry weight and wet weight, respectively.

2.9 Degradation

The GS/PEO hydrogels were immersed in PBS at 37 °C, with daily replacement of the PBS. The hydrogel samples were taken out at different time points (1, 3, 7, 14, and 21 d) for lyophilizing and weighing. The remaining mass (m_r, %) of the GS/PEO hydrogels was calculated as follows (Sang et al., 2023):

$$m_r = \frac{W_t}{W_0} \times 100\%, \tag{2}$$

where W_0 denotes the initial weight of the lyophilized samples, and W_t is the dry weight after several days of treatment with PBS.

2.10 Contact angle measurement

Water contact angles were measured via the sessile drop method. After 10 μL of deionized water was dropped on the surface of each GS/PEO hydrogel, measurements were taken using a Dino-Site digital microscope (AD 4113T, Taiwan, China), and the droplet morphology was recorded with a high-speed camera. The contact angle was analyzed in triplicate per sample using the Dino Capture 2.0 software.

2.11 Compression test

Compression tests were performed on GS/PEO hydrogels using a mechanical tester (INSTRON 3343, Norwood, MA, USA) to evaluate their mechanical properties. Cylindrical hydrogel samples were placed between the compression plates and compressed at a

rate of 0.8 mm/min. The compressive modulus was calculated from the linear region of the stress–strain curve within 10%–20% strain.

2.12 Rheological test

The rheological properties of the GS/PEO hydrogels were assessed using a rotational rheometer (Brookfield R/S Plus, USA). For viscosity measurements, 3 mL of hydrogel was loaded onto the testing plate and equilibrated at 25 ℃ for 10 min. The shear rate was swept from 0.01 to 1000 s^{-1}. To evaluate the viscoelastic behavior of hydrogels with different PEO concentrations, cylindrical samples (20 mm in diameter and 1 mm in height) were prepared. The storage modulus (G') and loss modulus (G'') were recorded in oscillatory mode over an angular frequency range of 0.1–100 rad/s. All oscillatory tests were conducted at 25 ℃, with a fixed frequency of 1 Hz and a strain amplitude of 0.1%.

2.13 Optimization of parameters and printability assessment of the GS/PEO bioinks

The parameter optimization and printability of GS/PEO ink were evaluated using a 3D-BioLab system (EnvisionTEC, Germany). During the printing process, the platform temperature was maintained at 10 ℃, the printing speed was 10 mm/s, and the nozzle diameter was 210 μm. The extrusion pressure was dynamically adjusted according to the requirements of different bioinks to produce printed lines with smooth surfaces and consistent widths. The diameters of the filaments under different conditions were measured using an optical microscope, and the degree of filament expansion (β) was calculated using Eq. (3) (Ning et al., 2020):

$$\beta = \frac{D_F}{D_N}, \tag{3}$$

where D_F denotes the actual filament diameter, and D_N is the theoretical diameter.

Multi-layer scaffolds were printed under optimal extrusion pressure, and quantitative analysis of the scaffolds was performed. According to the research of Seymour et al. (2021), the ink spreading degree (S_p) and window printability (P_w) of GS/PEO ink were calculated as follows:

$$S_p = \frac{S_t - S_a}{S_t} \times 100\%, \tag{4}$$

$$P_w = \frac{L^2}{16S_a}, \tag{5}$$

where S_t and S_a represent the theoretical and actual areas of the printed window, respectively, and L is the perimeter of the window.

2.14 3D bioprinting

Before printing, all devices were wiped with 75% (volume fraction) alcohol and exposed to UV light for 30 min to ensure sterility in the printing room. GS/1.5PEO ink was prepared, and a grid with a spacing of 1 mm (10 mm×10 mm) was printed at a pressure of 3.5 bar (1 bar=1×10^5 Pa) and a speed of 10 mm/s at 10 ℃. After the printing of each layer, it was irradiated with a UV curing lamp for 15 s. Finally, ATDC5 was seeded onto the scaffold at a density of 1×10^6 cells/cm^2 and cultured in DMEM/F12 medium containing 10% FBS and 1% penicillin/streptomycin. The medium was changed every two days.

2.15 Cell proliferation assay

The proliferation of ATDC5 in different hydrogel groups was evaluated on Days 1, 4, and 7 using the cell counting kit-8 (CCK-8; Abbkine, Wuhan, China). Samples were first rinsed with sterile PBS and then incubated with 300 μL of DMEM/F12 containing 10% (volume fraction) CCK-8 solution at 37 ℃ for 1.5 h. The supernatant was then transferred to a 96-well plate, and the optical density was measured at 450 nm using a Cytation 5 imaging reader (BioTek, USA).

2.16 Cell viability assay

For live/dead staining, scaffolds were immersed in PBS containing 2 μmol/L calcein acetoxymethyl ester (calcein-AM) at 37 ℃ for 30 min, rinsed twice with sterile PBS, and then incubated in PBS containing 4 μmol/L propidium iodide (PI) at 37 ℃ for 10 min. After staining, samples were washed with sterile PBS and imaged using a Cytation 5 imaging reader (BioTek). Live and dead cells were analyzed using ImageJ software, and cell viability was calculated as the percentage of live cells relative to the total number of cells.

2.17 Cell morphological analysis

On the fourth day of cultivation, the cell cytoskeleton was stained with phalloidin (Abbkine) and 4',6-diamidino-2-phenylindole (DAPI; Boster, Wuhan, China). Firstly, the cells were fixed with 4% (volume

fraction) paraformaldehyde solution (PFA) for 30 min and then permeabilized with PBS solution containing 0.1% (volume fraction) Triton X-100 for 20 min. Subsequently, the sample was stained with phalloidin in the dark for 30 min. Finally, the cell nucleus was stained with DAPI in the dark for 20 min. The scaffold was washed twice with PBS at the end of each step, for 5 min each time.

2.18 Immunofluorescence evaluation

Immunofluorescence was performed to evaluate the deposition of collagen II and aggrecan during cartilage formation and the differentiation process. After 14 d of cultivation, the scaffold was fixed in a 4% PFA for 30 min, permeabilized with 0.5% Triton X-100 for 15 min, and blocked with 5% (volume fraction) goat serum for 1 h. Then, primary antibodies were added, including rabbit anti-aggrecan polyclonal antibody (1:200 (volume ratio, the same below), ABclonal, China) and rabbit anti-collagen II polyclonal antibody (1:200, ABclonal), followed by incubation overnight at 4 ℃. Afterwards, the primary antibodies were aspirated and the scaffold was incubated with the secondary antibody (CY3-conjugated AffiniPure rabbit anti-goat immunoglobulin G (IgG) (H+L), 1:100, BA1034, Boster) at room temperature for 1 h. Finally, the cell nucleus was stained with DAPI solution for 30 min and the staining was evaluated using a Cytotion 5 imaging reader (BioTek).

2.19 Statistical analysis

All data were presented as mean±standard deviation. All the results were obtained in triplicate. Statistical analysis was performed using one-way analysis of variance (ANOVA), and $P<0.05$ was considered statistically significant.

3 Results and discussion

3.1 Preparation and characterization of the GS/PEO constructs

According to the GPC results, the weight-average molecular weight (M_w) of GelMA was 5629 g/mol, while the number-average molecular weight (M_n) was 4380 g/mol, with PDI of approximately 1.28. This indicates that GelMA has a narrow molecular weight distribution (Fig. 2a). Furthermore, the GPC chromatogram exhibited good separation and the sample components were relatively pure, with no significant impurity peaks or heterogeneous components observed. These results demonstrate that the synthesis of GelMA offers good controllability (Fig. 2b).

The FTIR results showed that the absorption peaks of PEO were mainly concentrated in the C–C bond stretching vibration at 2871 cm^{-1} and the C–O bond stretching vibration at 1094 cm^{-1}. These two peak segments of PEO disappeared in GS/0.5PEO, GS/1.0PEO, and GS/1.5PEO, indicating that the PEO had completely diminished (Fig. 2c).

The effect of PEO concentration on the fluidity of GS/PEO bioink was determined using the inversion test. The results showed that higher PEO concentrations led to slower flow of the GS/PEO bioink. The GS/0PEO bioink flowed immediately to the bottom upon inversion. In contrast, the GS/0.5PEO, GS/1.0PEO, and GS/1.5PEO bioinks flowed slowly down the sidewall after inversion. After 10 s of inversion, most of the GS/0.5PEO bioink had flowed to the bottom, with a small amount remaining on the sidewall, and the GS/1.0PEO bioink had just reached the bottom, while the GS/1.5PEO bioink continued to flow slowly along the sidewall (Fig. 2d).

The excellent hydrophilicity of hydrogels facilitates the transfer of nutrients, maintains humidity, and supports cell adhesion, proliferation, and migration within the hydrogel (Li et al., 2023). The water contact angles of GS/0PEO, GS/0.5PEO, GS/1.0PEO, and GS/1.5PEO were measured to be 52.5°, 39.1°, 25.8°, and 12.8°, respectively, demonstrating a clear trend of improved hydrophilicity with increasing PEO concentration (Fig. 2e). The surface morphology of GS/PEO hydrogels revealed that after PEO leaching, a large number of pores were left on the hydrogel surface and the pore size increased with a higher PEO content (Figs. 2f and S1). These pores facilitate water penetration into the hydrogel, allowing polar functional groups, such as amide, carboxyl, and hydroxyl groups, in the GelMA/SF hydrogel to interact more effectively with water molecules (Lu et al., 2022). The resulting reduction in contact angle and improved surface hydrophilicity promote nutrient transport and ultimately support cell proliferation.

The interconnected porous structure within the hydrogel scaffold plays a critical role in supporting ECM secretion, nutrient and waste transport, and cell proliferation. SEM images revealed that the incorporation

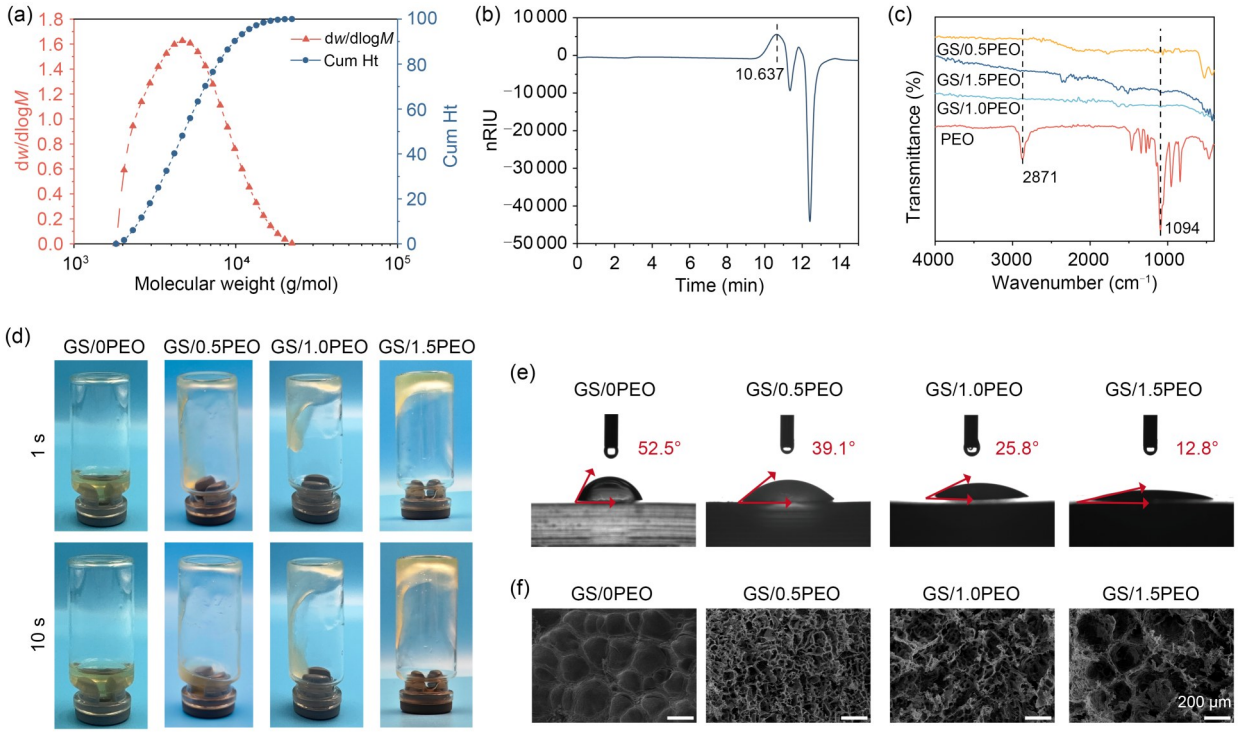

Fig. 2 Material characterization. (a) Gel permeation chromatography (GPC) profile of gelatin methacrylate (GelMA): molecular weight distribution curve and cumulative distribution curve. (b) Chromatogram of GelMA. (c) Fourier transform infrared (FTIR) spectra of GS/PEO hydrogels. (d) Fluidity of GS/PEO bioinks with different concentrations. (e) Water contact angle test for GS/PEO hydrogel surfaces. (f) Surface morphology images of the GS/PEO hydrogels. G: gelatin methacrylate; S: silk fibroin; PEO: polyethylene oxide; d*w*/dlog*M*: weight fraction derivative with respect to the logarithm of molecular weight; Cum Ht: cumulative height; nRIU: nano refractive index unit.

of PEO led to the formation of highly interconnected and size-tunable micropores within the composite hydrogel (Fig. 3a). Both pore size and porosity increased with rising PEO concentration, with averages of (57.29±21.62) μm and 22.67% for GS/0PEO, (83.48±28.16) μm and 42.07% for GS/0.5PEO, (121.99±25.25) μm and 62.85% for GS/1.0PEO, and (157.77±18.06) μm and 88.39% for GS/1.5PEO, respectively (Figs. 3a and 3b). This phenomenon can be attributed to the formation of spherical PEO droplets within the precursor solution. As the PEO concentration increased, the droplet size grew, resulting in the coalescence of adjacent droplets. Upon the removal of PEO, larger pores were left behind in the hydrogel matrix (Li et al., 2022).

The mechanical properties of cartilage tissue engineering scaffolds are crucial for determining the application of such scaffolds (Appel et al., 2015; Wang et al., 2021). Cartilage substitutes require scaffolds to have the ability to resist abrasion caused by movement or pressure from surrounding tissues (Pattanashetti et al., 2020). The stress–strain curves and compressive moduli are shown in Figs. 3c and 3d. The addition of PEO led to greater deformation of the hydrogel under the same stress conditions, and the compressive modulus of GelMA was (25.31±1.08) kPa. In contrast, GelMA/0.5PEO exhibited a lower modulus of (15.22±2.11) kPa, indicating that the introduction of PEO reduced the mechanical properties of the GelMA hydrogel. By comparison, the compressive modulus of the GS/0PEO hydrogel reached (45.12±2.60) kPa, suggesting that the addition of SF effectively enhanced the stiffness of GelMA. Moreover, relative to GelMA/0.5PEO, the GS/0.5PEO hydrogel showed an increase of approximately 22 kPa. These results demonstrate that in GS/PEO hydrogels, the incorporation of SF compensates for the mechanical loss induced by PEO. This effect is likely attributed to the formation of interpenetrating polymer networks (IPNs) between SF and GelMA, which stabilizes the hydrogel network and enhances its mechanical strength (Zheng et al., 2023). In fact, the compressive modulus

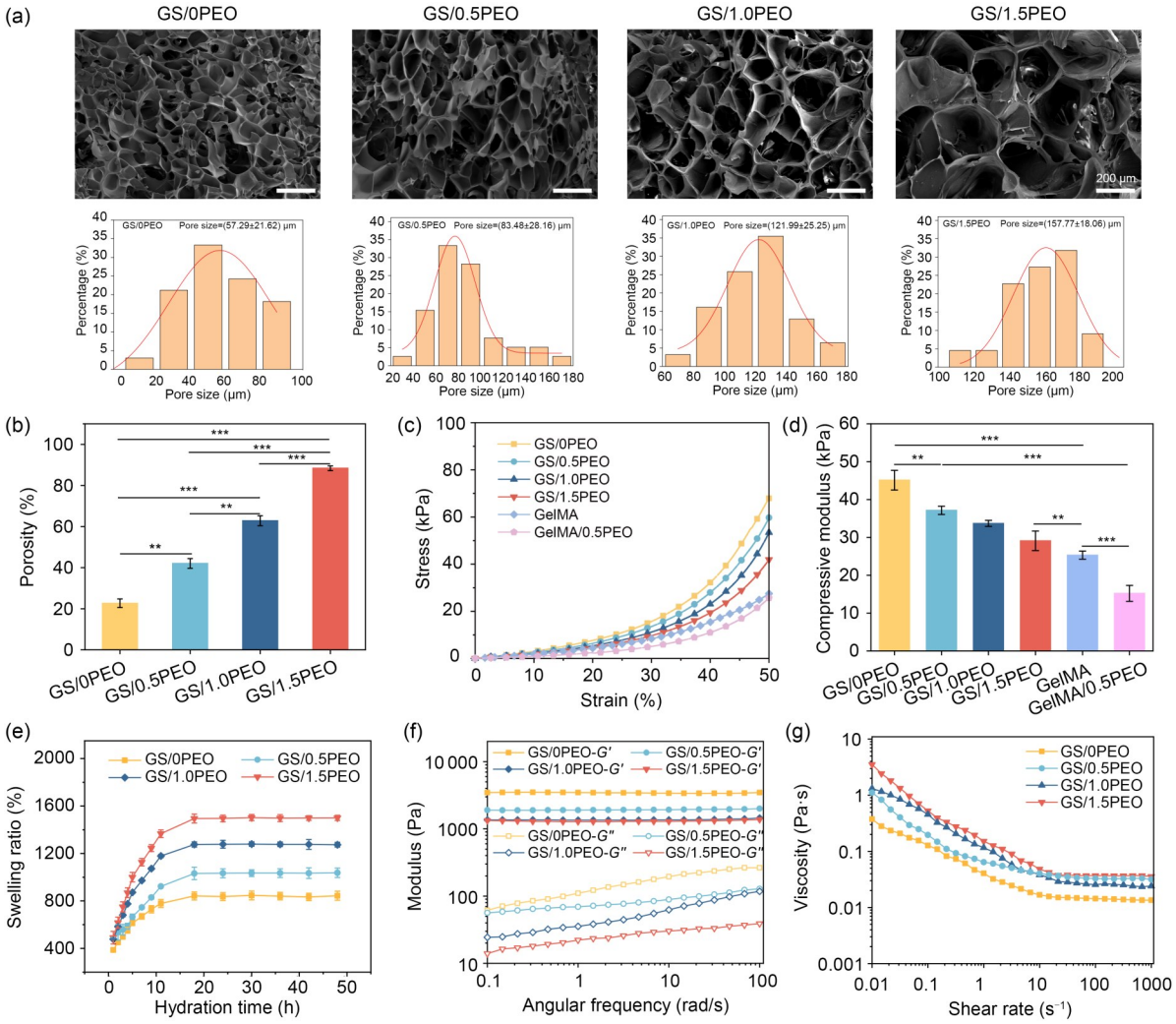

Fig. 3 Characterization and properties of GS/PEO hydrogels. (a) Scanning electron microscopy (SEM) images and pore size quantification of hydrogels. (b) Porosity. (c) Stress–strain curves. (d) Compressive modulus. (e) Swelling ratio. (f) Storage modulus (*G′*) and loss modulus (*G″*). (g) Viscosity. (b, d, e) The data are expressed as mean±standard deviation (SD), *n*=3. ** *P*<0.01, * *P*<0.001. GelMA, G: gelatin methacrylate; S: silk fibroin; PEO: polyethylene oxide.**

of hydrogels should closely match that of native cartilage to preserve the chondrocyte phenotype (Zhang and Yu, 2025). The compressive modulus of articular cartilage ranges from 0.02–1.16 MPa in the superficial zone to 6.44–7.75 MPa in the deep zone, and scaffolds with a modulus within this optimal range have been reported to support superior chondrogenic function. Among the GS/PEO hydrogels, GS/1.5PEO exhibited a compressive modulus of (29.10±2.59) kPa, comparable to that of GelMA, which corresponds to the cartilage superficial zone and suggests its suitability for cartilage formation.

The swelling behavior of GS/PEO hydrogels is shown in Fig. 3e. Hydrogels with higher PEO concentrations exhibited greater swelling ratios, and all samples reached equilibrium within approximately 20 h. Notably, the incorporation of PEO significantly enhanced the swelling capacity compared to the PEO-free hydrogel. The swelling ratio increased with PEO concentration, reaching 1500.04% for GS/1.5PEO, 1280.91% for GS/1.0PEO, 1037.44% for GS/0.5PEO, and 847.41% for GS/0PEO.

In order to investigate the persistence of mechanical strength of the scaffold, we studied the degradation of GS/PEO hydrogels in PBS and measured the degradation rate over time based on the remaining mass. As shown in Fig. S2, the remaining mass of the GS/PEO hydrogels kept stable throughout the 21-d degradation period, indicating a highly stable material structure without significant degradation. Therefore, the

mechanical strength of the hydrogel scaffold can be consistently maintained.

In order to evaluate the suitability of GS/PEO bioinks for extrusion printing, their rheological properties, including viscosity and viscoelasticity, were measured. The viscoelasticity test results indicated that G' and G'' of the GS/PEO bioinks decreased with increasing PEO content. In all bioinks, the G' values were significantly greater than the G'' values, indicating elastic and highly structured properties after crosslinking. This suggests that these bioinks maintain favorable shape fidelity after printing (Fig. 3f). Fig. 3g shows the variation in GS/PEO bioink viscosity with the shear rate. It can be observed that the viscosity of these bioinks decreases as the shear rate increases, demonstrating typical shear-thinning behavior. This is a crucial property for extrusion-based printing processes, as it facilitates ink flow during extrusion and enables the rapid recovery of structural strength after deposition. More importantly, the PEO concentration significantly influenced the fluidity of the GS/PEO bioinks. As the amount of PEO increased, the viscosity of the bioinks also increased, correspondingly reducing their fluidity. Specifically, GS/0PEO exhibited the lowest viscosity (0.37 Pa·s) and the highest fluidity. After adding PEO, the viscosity gradually increased: GS/0.5PEO showed a viscosity of 1.11 Pa·s, GS/1.0PEO 1.32 Pa·s, while GS/1.5PEO reached the highest viscosity (3.53 Pa·s) and the lowest fluidity. These results demonstrate that the addition of PEO not only preserved the shear-thinning behavior but also significantly increased the overall viscosity of the bioink, reduced the fluidity, and further optimized the printability of the GS/PEO bioink (Isreb et al., 2019).

3.2 Printability analysis of the GS/PEO inks

To study the effects of molecular weight on the pore size and porosity of hydrogels, we prepared GS/1.0PEO$_{MW=12\,000}$, GS/1.0PEO$_{MW=100\,000}$, GS/1.0PEO$_{MW=300\,000}$ hydrogels. The internal structure, pore size, and porosity of the GS/1.0PEO hydrogel, shown in Figs. 4a and 4b, increased with the increase in PEO molecular weight, because the higher the molecular weight of PEO, the more it tends to aggregate and form larger emulsion droplets. Consequently, the pores left behind after sacrificing the PEO become larger (Yi et al., 2022).

Next, we systematically studied the effects of different molecular weights on ink printing performance by adjusting the extrusion pressure (1.8–2.2 bar) and printing speed (8–12 mm/s) under the conditions of a nozzle diameter of 210 μm and a platform temperature of 10 ℃. The printed results were recorded, divided into three groups, and marked with corresponding colors (Fig. 4c). The printability diagram shows that the larger the molecular weight is, the smaller the printability parameter range of GS/1.0PEO bioink. This is because the larger the molecular weight of PEO is, the greater the viscosity of GS/1.0PEO hydrogel; besides, the material flow in the 3D printer nozzle is limited, which hinders the printing of GS/1.0PEO bioink (Isreb et al., 2019).

In order to achieve high shape fidelity in 3D-bioprinted structures, we optimized the printing parameters and evaluated the printability of GS/PEO bioinks. During the extrusion process, different extrusion pressures cause significant extrusion swelling effects in the bioink, which in turn affects the accuracy of the printing structure being formed (Fig. 5a). To quantify this phenomenon, we explored the expansion of the filament under different extrusion pressures (1.5 to 3.5 bar) using a 210 μm diameter nozzle and a printing speed of 10 mm/s at 10 ℃ and expressed the expansion using the β value. High print fidelity is observed when the β value is equal to or close to 1; conversely, values that substantially deviate from 1 result in decreased printing precision (Ning et al., 2020). As seen in Figs. 5b and 5c, the filament diameter and β value increase with higher extrusion pressure. At the same extrusion pressure, the filament diameter decreases with increasing PEO concentration. From the optical images of the filaments at different extrusion pressures, we could observe that GS/0PEO can produce continuous and uniform filaments under extrusion pressures ranging from 1.5 to 3.5 bar. GS/0.5PEO cannot produce continuous filaments at 1.5 bar, and when the extrusion pressure exceeds 2.5 bar, the filaments become uneven and rough. However, filaments printed at 2.0 bar meet the requirements for continuity and uniformity. GS/1.0PEO produces continuous and uniform filaments at extrusion pressures of 2.5 and 3.0 bar, while GS/1.5PEO can only produce continuous and uniform filaments at an extrusion pressure of 3.5 bar (Fig. S3). Therefore, after considering the continuity, uniformity, and β values, we determined the optimal extrusion pressures for the different materials as follows: GS/0PEO at 1.5 bar, GS/0.5PEO at 2.0 bar, GS/1.0PEO at 2.5 bar, and GS/1.5PEO at 3.5 bar.

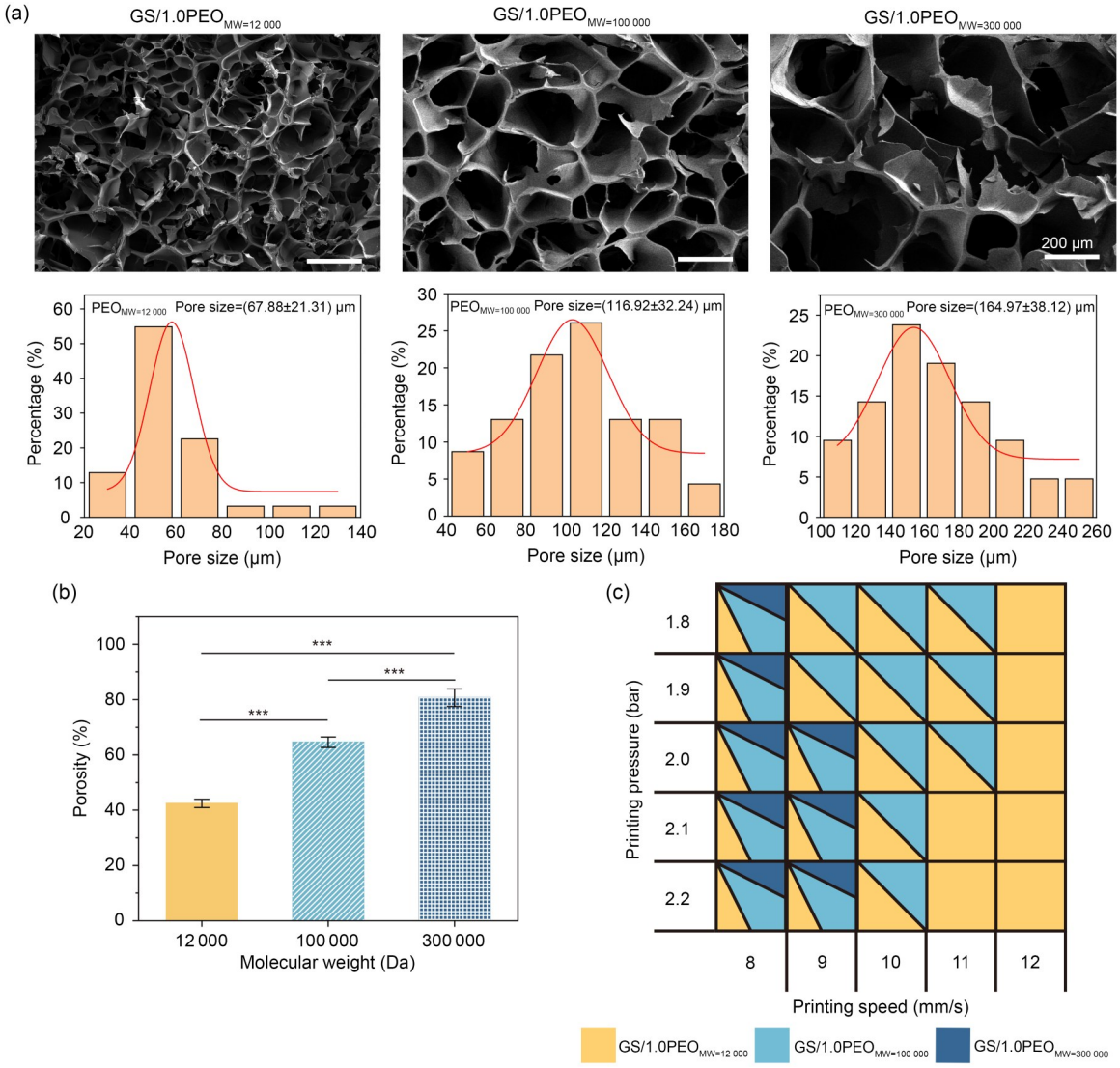

Fig. 4 Characterization and printability of GS/1.0PEO hydrogels with different molecular weights. (a) Scanning electron microscopy (SEM) images and pore size. (b) Porosity. The data are expressed as mean±standard deviation (SD), n=3. *** P< 0.001. (c) Printability map showing the printable parameters of bioinks. G: gelatin methacrylate; S: silk fibroin; PEO: polyethylene oxide; MW: molecular weight. 1 bar=1×10^5 Pa.

In the actual printing process, the intersection of two filaments will diffuse due to gravity, resulting in the S_a of the window being smaller than the S_t (Fig. 5d) (Seymour et al., 2021). We evaluated the properties of four different inks using S_p as an indicator. Fig. 5e showed that the spreading degree of the GS/0PEO group is the highest (61.73%). After the addition of PEO, the spreading degree decreases, indicating that the ink has greater shape fidelity after adding PEO. It can also be observed from the figure that there is no significant difference in the spreading degree of the three groups of bioinks: GS/0.5PEO (55.17%), GS/1.0PEO (53.58%), and GS/1.5PEO (52.86%). Under the optimal extrusion pressure conditions, multi-layer scaffolds (1000 μm distance) were printed using GS/PEO inks of different formulations. Subsequently, the P_w values were calculated from the optical images of the 2-layer scaffolds (Fig. S4). The P_w values of GS/0PEO, GS/0.5PEO, GS/1.0PEO, and GS/1.5PEO were 1.020±0.011, 1.024±0.022, 1.028±0.029, and 1.039±0.044, respectively. These values are approximately equal to 1 (Fig. 5f). According to earlier research (Seymour et al., 2021), all four types of ink are capable of creating perfectly square windows.

The images of the 10-layer scaffold show that the surface of GS/0PEO is severely irregular, resulting in

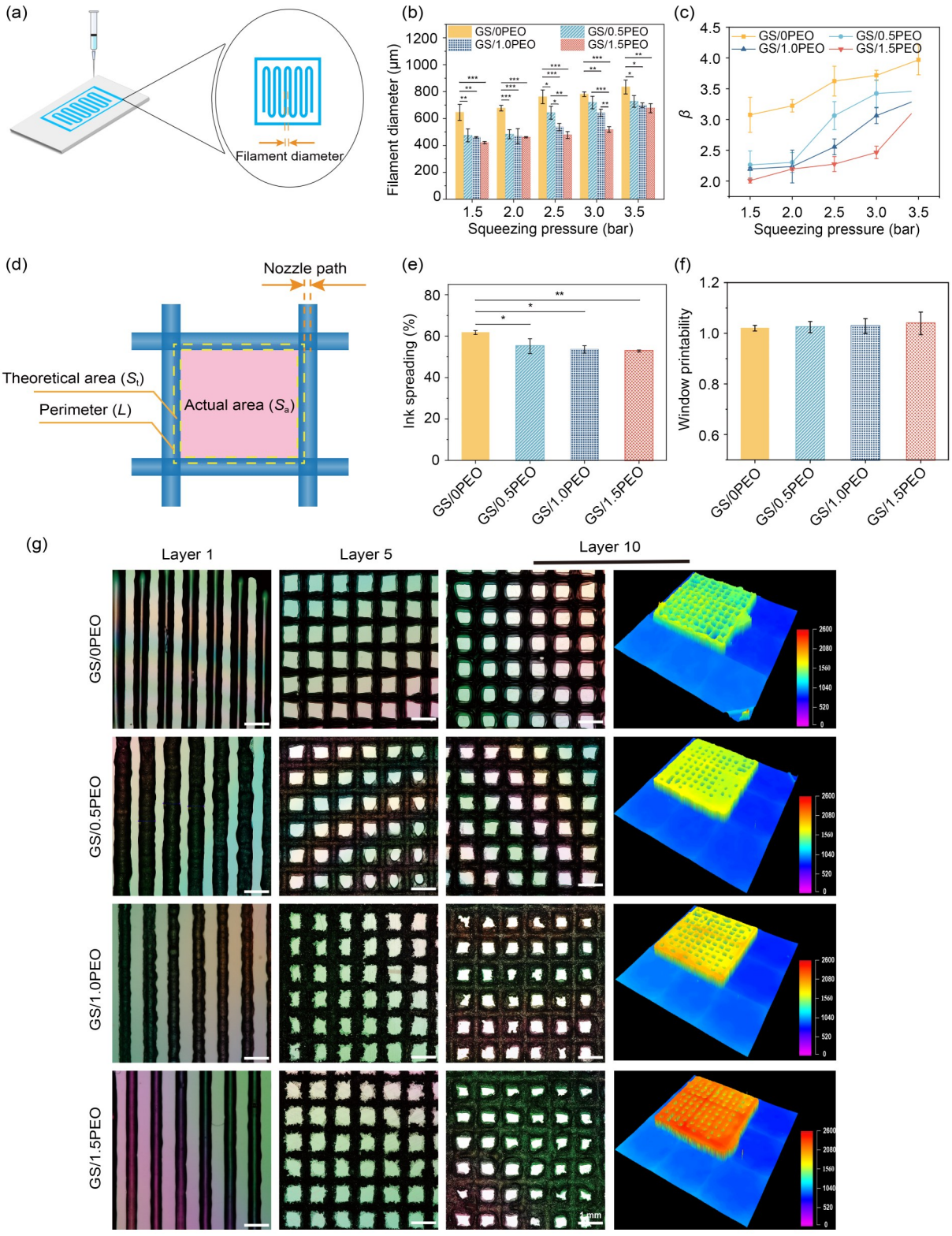

Fig. 5 Printing suitability analysis of GS/PEO ink. (a) Schematic diagram of the sedimentation process. (b) Filament diameter under different pressures. (c) Filament expansion degree (β). (d) Schematic diagram of research on ink spreading and window printability. (e) Ink spreading degree (S_p). (f) Window printability (P_w). (g) Optical images of the lattice scaffold. The data are expressed as mean±standard deviation (SD), n=3. $^{*}P$<0.05, $^{**}P$<0.01, $^{***}P$<0.001. G: gelatin methacrylate; S: silk fibroin; PEO: polyethylene oxide. 1 bar=1×10^5 Pa.

poor print quality and indicating its low printability (Fig. 5g). However, the addition of PEO has significantly improved the stacking performance. Among the tested formulations, GS/1.5PEO exhibited the highest stacking height and the best shape fidelity, significantly outperforming other ratios (GS/0.5PEO and GS/1.0PEO). Therefore, GS/1.5PEO was identified as the optimal choice.

3.3 Biocompatibility of the porous hydrogel scaffold

The biocompatibility of GS/PEO hydrogels was evaluated using CCK-8, live/dead staining, and cytoskeleton staining. On the 4th and 7th days, all GS/PEO hydrogels showed high cell proliferation rates (Fig. 6a). Throughout the 7-d culture period, very few dead cells were observed on the surface of all GS/PEO hydrogels (Fig. 6b). With the number of culture days passing, the cell number gradually increased, and cell aggregation was observed, with a survival rate of up to 94% (Fig. 6c). This indicates that none of the GS/PEO hydrogels exhibited cytotoxicity and could support normal cell proliferation and metabolism. Additionally, it was observed that as the PEO concentration increased, the number of live cells on the hydrogels also increased. This is because with the pore size and porosity of GS/PEO hydrogel becoming larger, the transport of nutrients and metabolic waste is enhanced, thus creating a more favorable environment for cell proliferation. In addition, the promotive effect of PEO on cell proliferation might also be related to the modulus of GS/PEO hydrogel. Rheological analysis revealed that a higher PEO content led to a lower storage modulus of the hydrogels (Fig. 3f). A reduced storage modulus has been reported to correspond to a faster relaxation rate, and such rapidly relaxing hydrogels enhance cell–matrix interactions, thereby alleviating excessive actin activation and apoptosis, ultimately supporting long-term cartilage formation (Huang et al., 2023). On the 4th and 7th days, the GS/1.5PEO hydrogels exhibited the highest number of live cells. After 4 d of culture, ATDC5 cells were firmly attached to the surface of each hydrogel, with cells evenly distributed across the surface at a moderate density. ATDC5 cells showed a polygonal distribution (Fig. 6d). On the basis of GS/PEO hydrogel characterization, printability, and biocompatibility, GS/1.5PEO bioink was selected for further experiments.

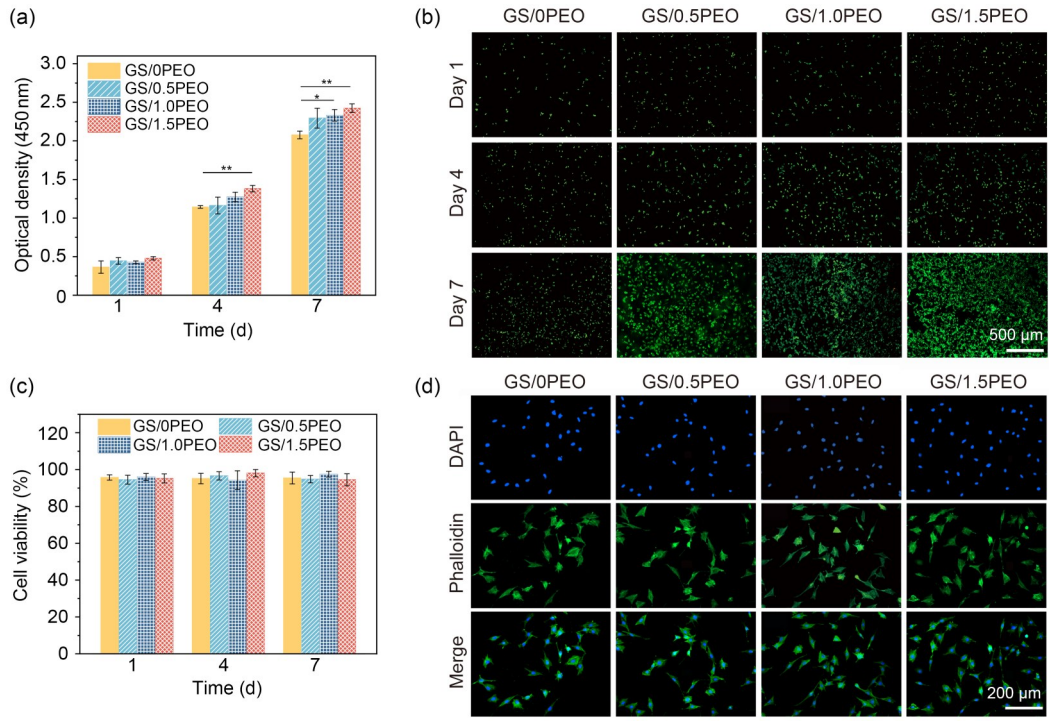

Fig. 6 Biocompatibility of GS/PEO hydrogels. (a) Optical density at 450 nm. (b) Live/dead staining on Days 1, 4, and 7. (c) Cell viability. (d) Skeleton staining on Day 4. The data are expressed as mean±standard deviation (SD), n=3. $^{*}P$<0.05, $^{**}P$<0.01. G: gelatin methacrylate; S: silk fibroin; PEO: polyethylene oxide; DAPI: 4',6-diamidino-2-phenylindole.

3.4 Cell behavior on the 3D scaffold

In order to evaluate the behavior of cells on 3D scaffolds, a 3D scaffold was printed using GS/1.5PEO ink and ATDC5 was seeded onto its surface. The proliferation of cells on 3D GS/1.5PEO scaffolds is shown in Fig. 7a. The number of live cells was relatively small on Day 1, but as the culture days passed, the number of cells gradually increased. On Day 7, the scaffold was covered by cells, suggesting that the 3D scaffold constructed with GS/1.5PEO ink could effectively maintain the adhesion stability of cells and promote their growth. The skeleton staining results revealed that the cell morphology is intact and normal, further confirming that the 3D scaffold constructed with GS/1.5PEO can support cell growth (Fig. 7b). As shown in Fig. 7c, large amounts of collagen II and aggrecan have been deposited on the scaffold, with collagen II being the main structural protein of the cartilage matrix, providing mechanical support, and aggrecan being the main proteoglycan in the cartilage matrix, which is responsible for maintaining moisture and compression strength. This indicates that our scaffold can promote the secretion of cartilage matrix components by chondrocytes during culture and also suggests that chondrocytes begin to transform into articular cartilage on Day 14.

4 Conclusions

In order to address the issue that pure GelMA cannot balance high biocompatibility and high mechanical strength, in this study, we developed a composite bioink GS/PEO based on GelMA, SF, and PEO. The characterization of the GS/PEO bioink showed that PEO acts as a porogen, generating a highly porous structure with a porosity of up to 88%, while SF compensates for the mechanical loss caused by PEO, allowing the scaffold to maintain a compression strength

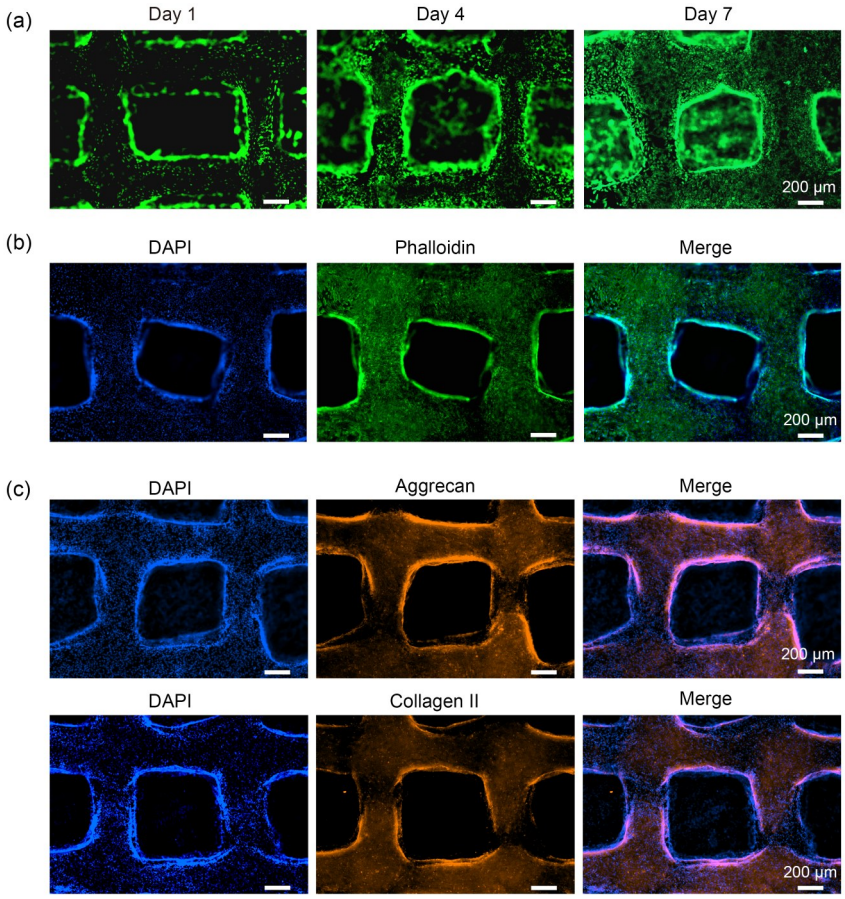

Fig. 7 Behavior of cells on 3D scaffolds. (a) Live/dead staining. (b) Skeleton staining. (c) Immunofluorescence staining of aggrecan and collagen II. DAPI: 4',6-diamidino-2-phenylindole.

of up to 29.10 kPa. Among the tested formulations, the GS/1.5PEO bioink exhibited excellent printability, mechanical integrity, and cytocompatibility, and it supported the firm deposition of collagen II and aggregation by chondrocytes after printing. Overall, the novel GS/PEO bioink developed in this study balances biocompatibility and mechanical strength, with significant prospective applications in cartilage tissue engineering.

Data availability statement

The data will be made available upon request.

Acknowledgments

This work was supported by the Project (No. JCKY2024 408C010), the Shanxi Province Key Research and Development Project (No. 202302130501006), the National Natural Science Foundation of China (Nos. 82403350, 51975400, and 62031022), the Shanxi Provincial Key Medical Scientific Research Project (No. 2020XM06), the Shanxi Provincial Basic Research Project (No. 202103021223040), the Scientific and Technological Innovation Programs of Higher Education Institutions in Shanxi (No. 2021L044), and the Shanxi-Zheda Institute of Advanced Materials and Chemical Engineering (No. 2022SX-TD026), China.

Author contributions

Zijun MA: conceptualization, investigation, methodology, writing – original draft, validation, and data curation. Meng LI: validation and writing – review & editing. Wendan JIA: data curation and resources. Xiaoyuan WANG and Lu HAN: validation and investigation. Rong CHENG: validation and resources. Shengbo SANG: conceptualization, writing – review & editing, supervision, and funding acquisition. Xiaoning YANG: writing – review & editing and methodology. All authors have read and approved the final manuscript, and therefore, have full access to all the data in the study and take responsibility for the integrity and security of the data.

Compliance with ethics guidelines

Zijun MA, Wendan JIA, Xiaoyuan WANG, Rong CHENG, Lu HAN, Meng LI, Xiaoning YANG, and Shengbo SANG declare that they have no conflicts of interest.

This article does not contain any studies with human or animal subjects performed by any of the authors.

References

Appel EA, Tibbitt MW, Webber MJ, et al., 2015. Self-assembled hydrogels utilizing polymer–nanoparticle interactions. *Nat Commun*, 6:6295. https://doi.org/10.1038/ncomms7295

Arguchinskaya NV, Isaeva EV, Kisel AA, et al., 2023. Properties and printability of the synthesized hydrogel based on GeLMA. *Int J Mol Sci*, 24(3):2121. https://doi.org/10.3390/ijms24032121

Bai L, Jing YY, Reis RL, et al., 2025. Organoid research: theory, technology, and therapeutics. *Organoid Res*, 1(1): 025040007. https://doi.org/10.36922/or025040007

Brunel LG, Hull SM, Heilshorn SC, 2022. Engineered assistive materials for 3D bioprinting: support baths and sacrificial inks. *Biofabrication*, 14(3):032001. https://doi.org/10.1088/1758-5090/ac6bbe

Cao YY, Cheng P, Sang SB, et al., 2021. 3D printed PCL/GelMA biphasic scaffold boosts cartilage regeneration using co-culture of mesenchymal stem cells and chondrocytes: *in vivo* study. *Mater Des*, 210:110065. https://doi.org/10.1016/j.matdes.2021.110065

Chen SS, Wang Y, Lai JH, et al., 2023. Structure and properties of gelatin methacryloyl (GelMA) synthesized in different reaction systems. *Biomacromolecules*, 24(6): 2928-2941. https://doi.org/10.1021/acs.biomac.3c00302

de Girolamo L, Ragni E, Cucchiarini M, et al., 2019. Cells, soluble factors and matrix harmonically play the concert of allograft integration. *Knee Surg Sports Traumatol Arthrosc*, 27(6):1717-1725. https://doi.org/10.1007/s00167-018-5182-1

Findeisen S, Gräfe N, Schwilk M, et al., 2023. Use of autologous bone graft with bioactive glass as a bone substitute in the treatment of large-sized bone defects of the femur and tibia. *J Pers Med*, 13(12):1644. https://doi.org/10.3390/jpm13121644

He P, Zhao YB, Wang B, et al., 2024. A biodegradable magnesium phosphate cement incorporating chitosan and rhBMP-2 designed for bone defect repair. *J Orthop Transl*, 49: 167-180. https://doi.org/10.1016/j.jot.2024.08.004

Hou MZ, Zhang YJ, Liu Y, et al., 2023. Biomimetic melatonin-loaded silk fibroin/GelMA scaffold strengthens cartilage repair through retrieval of mitochondrial functions. *J Mater Sci Technol*, 146:102-112. https://doi.org/10.1016/j.jmst.2022.10.031

Huang DY, Li YH, Ma ZH, et al., 2023. Collagen hydrogel viscoelasticity regulates MSC chondrogenesis in a ROCK-dependent manner. *Sci Adv*, 9(6):eade9497. https://doi.org/10.1126/sciadv.ade9497

Isreb A, Baj K, Wojsz M, et al., 2019. 3D printed oral theophylline doses with innovative 'radiator-like' design: impact of polyethylene oxide (PEO) molecular weight. *Int J Pharm*, 564:98-105. https://doi.org/10.1016/j.ijpharm.2019.04.017

Jeong SH, Hiemstra J, Blokzijl PV, et al., 2024. An oxygenating colloidal bioink for the engineering of biomimetic tissue constructs. *Bio-Des Manuf*, 7(3):240-261. https://doi.org/10.1007/s42242-024-00281-7

Jia LT, Hua YJ, Zeng JS, et al., 2022. Bioprinting and

regeneration of auricular cartilage using a bioactive bioink based on microporous photocrosslinkable acellular cartilage matrix. *Bioact Mater*, 16:66-81. https://doi.org/10.1016/j.bioactmat.2022.02.032

Lee SS, Du XY, Kim I, et al., 2022. Scaffolds for bone-tissue engineering. *Matter*, 5(9):2722-2759. https://doi.org/10.1016/j.matt.2022.06.003

Li M, Sun L, Liu ZX, et al., 2023. 3D bioprinting of heterogeneous tissue-engineered skin containing human dermal fibroblasts and keratinocytes. *Biomater Sci*, 11(7):2461-2477. https://doi.org/10.1039/d2bm02092k

Li M, Liu ZX, Shen ZZ, et al., 2024. A heparin-functionalized bioink with sustained delivery of vascular endothelial growth factor for 3D bioprinting of prevascularized dermal constructs. *Int J Biol Macromol*, 262:130075. https://doi.org/10.1016/j.ijbiomac.2024.130075

Li MX, Song P, Wang WZ, et al., 2022. Preparation and characterization of biomimetic gradient multi-layer cell-laden scaffolds for osteochondral integrated repair. *J Mater Chem B*, 10(22):4172-4188. https://doi.org/10.1039/d2tb00576j

Liu M, Zeng X, Ma C, et al., 2017. Injectable hydrogels for cartilage and bone tissue engineering. *Bone Res*, 5:17014. https://doi.org/10.1038/boneres.2017.14

Liu Y, Yu L, Zhang D, et al., 2022. Manufacture and preliminary evaluation of acellular tooth roots as allografts for alveolar ridge augmentation. *J Biomed Mater Res A*, 110:122-130. https://doi.org/10.1002/jbm.a.37270

Lu XT, Song WJ, Sun XM, et al., 2022. Porous hydrogel constructs based on methacrylated gelatin/polyethylene oxide for corneal stromal regeneration. *Mater Today Commun*, 32:104071. https://doi.org/10.1016/j.mtcomm.2022.104071

Ma WP, Lu HX, Xiao Y, et al., 2025. Advancing organoid development with 3D bioprinting. *Organoid Res*, 1(1): 025040004. https://doi.org/10.36922/or025040004

Manohar SS, Das C, Kakati V, 2024. Bone tissue engineering scaffolds: materials and methods. *3D Print Addit Manuf*, 11(1):347-362. https://doi.org/10.1089/3dp.2022.0216

Müller SA, Barg A, Vavken P, et al., 2016. Autograft versus sterilized allograft for lateral calcaneal lengthening osteotomies. *Medicine*, 95(30):e4343. https://doi.org/10.1097/md.0000000000004343

Ng WL, Huang X, Shkolnikov V, et al., 2023. Polyvinylpyrrolidone-based bioink: influence of bioink properties on printing performance and cell proliferation during inkjet-based bioprinting. *Bio-Des Manuf*, 6(6):676-690. https://doi.org/10.1007/s42242-023-00245-3

Ning LQ, Mehta R, Cao C, et al., 2020. Embedded 3D bioprinting of gelatin methacryloyl-based constructs with highly tunable structural fidelity. *ACS Appl Mater Interfaces*, 12(40):44563-44577. https://doi.org/10.1021/acsami.0c15078

Pattanashetti NA, Viana T, Alves N, et al., 2020. Development of novel 3D scaffolds using BioExtruder by varying the content of hydroxyapatite and silica in PCL matrix for bone tissue engineering. *J Polym Res*, 27(4):87. https://doi.org/10.1007/s10965-020-02053-0

Sang SB, Mao XJ, Cao YY, et al., 2023. 3D bioprinting using synovium-derived MSC-laden photo-cross-linked ECM bioink for cartilage regeneration. *ACS Appl Mater Interfaces*, 15(7):8895-8913. https://doi.org/10.1021/acsami.2c19058

Seymour AJ, Shin S, Heilshorn SC, 2021. 3D printing of microgel scaffolds with tunable void fraction to promote cell infiltration. *Adv Healthc Mater*, 10(18):2100644. https://doi.org/10.1002/adhm.202100644

Sharifi S, Sharifi H, Akbari A, et al., 2021. Systematic optimization of visible light-induced crosslinking conditions of gelatin methacryloyl (GelMA). *Sci Rep*, 11:23276. https://doi.org/10.1038/s41598-021-02830-x

Shi XH, Bai Y, He XM, et al., 2022. Shaoyao Gancao Decoction for limb dysfunction after fractures around the knee. *Medicine*, 101(11):e29051. https://doi.org/10.1097/md.0000000000029051

Tuchman A, Brodke DS, Youssef JA, et al., 2016. Iliac crest bone graft versus local autograft or allograft for lumbar spinal fusion: a systematic review. *Global Spine J*, 6(6): 592-606. https://doi.org/10.1055/s-0035-1570749

Verma V, Verma P, Kar S, et al., 2007. Fabrication of agar-gelatin hybrid scaffolds using a novel entrapment method for in vitro tissue engineering applications. *Biotechnol Bioeng*, 96(2):392-400. https://doi.org/10.1002/bit.21111

Wang C, Huang W, Zhou Y, et al., 2020. 3D printing of bone tissue engineering scaffolds. *Bioact Mater*, 5(1):82-91. https://doi.org/10.1016/j.bioactmat.2020.01.004

Wang WZ, Zhang BQ, Li MX, et al., 2021. 3D printing of PLA/n-HA composite scaffolds with customized mechanical properties and biological functions for bone tissue engineering. *Compos Part B Eng*, 224:109192. https://doi.org/10.1016/j.compositesb.2021.109192

Wang YT, Hou Y, Hao T, et al., 2024. Model construction and clinical therapeutic potential of engineered cardiac organoids for cardiovascular diseases. *Biomater Transl*, 5(4): 337-354. https://doi.org/10.12336/biomatertransl.2024.04.002

Wang Z, Wang X, Huang Y, et al., 2024. $Ca_v3.3$-mediated endochondral ossification in a three-dimensional bioprinted GelMA hydrogel. *Bio-Des Manuf*, 7(6):983-999. https://doi.org/10.1007/s42242-024-00287-1

Xia YL, Wang HY, Li YH, et al., 2022. Engineered bone cement trigger bone defect regeneration. *Front Mater*, 9: 929618. https://doi.org/10.3389/fmats.2022.929618

Xie MJ, Gao Q, Zhao HM, et al., 2019. Electro-assisted bioprinting of low-concentration GelMA microdroplets. *Small*,

15(4):1804216.
https://doi.org/10.1002/smll.201804216

Xue NN, Ding XF, Huang RZ, et al., 2022. Bone tissue engineering in the treatment of bone defects. *Pharmaceuticals*, 15(7):879.
https://doi.org/10.3390/ph15070879

Xue YM, Kim HJ, Lee J, et al., 2022. Co-electrospun silk fibroin and gelatin methacryloyl sheet seeded with mesenchymal stem cells for tendon regeneration. *Small*, 18(21): 2107714.
https://doi.org/10.1002/smll.202107714

Yang JR, He HM, Li D, et al., 2023. Advanced strategies in the application of gelatin-based bioink for extrusion bioprinting. *Bio-Des Manuf*, 6(5):586-608.
https://doi.org/10.1007/s42242-023-00236-4

Yi SL, Liu Q, Luo ZY, et al., 2022. Micropore-forming gelatin methacryloyl (GelMA) bioink toolbox 2.0: designable tunability and adaptability for 3D bioprinting applications. *Small*, 18(25):2106357.
https://doi.org/10.1002/smll.202106357

Ying GL, Jiang N, Maharjan S, et al., 2018. Aqueous two-phase emulsion bioink-enabled 3D bioprinting of porous hydrogels. *Adv Mater*, 30(50):1805460.
https://doi.org/10.1002/adma.201805460

Yuan X, Zhu W, Yang ZY, et al., 2024. Recent advances in 3D printing of smart scaffolds for bone tissue engineering and regeneration. *Adv Mater*, 36(34):2403641.
https://doi.org/10.1002/adma.202403641

Zhang LY, Bi Q, Zhao C, et al., 2020. Recent advances in biomaterials for the treatment of bone defects. *Organogenesis*, 16(4):113-125.
https://doi.org/10.1080/15476278.2020.1808428

Zhang YS, Yu WH, 2025. Recent advances in bionic scaffolds for cartilage tissue engineering. *Front Bioeng Biotechnol*, 13:1625550.
https://doi.org/10.3389/fbioe.2025.1625550

Zhang YW, Li ZX, Guan JJ, et al., 2021. Hydrogel: a potential therapeutic material for bone tissue engineering. *AIP Adv*, 11(1):010701.
https://doi.org/10.1063/5.0035504

Zheng KW, Zheng X, Yu MZ, et al., 2023. BMSCs-seeded interpenetrating network GelMA/SF composite hydrogel for articular cartilage repair. *J Funct Biomater*, 14(1):39.
https://doi.org/10.3390/jfb14010039

Supplementary information

Figs. S1–S4